POLITECNICO DI TORINO
Repository ISTITUZIONALE

Emerging Spatiotemporal Dynamics in Multiterminal Neuromorphic Nanowire Networks Through Conductance Matrices and Voltage Maps

Terms of use:

(Article begins on next page)

18 November 2024

RESEARCH ARTICLE

ADVANCED
ELECTRONIC
MATERIALS
Open Access

www.advelectronicmat.de

Emerging Spatiotemporal Dynamics in Multiterminal Neuromorphic Nanowire Networks Through Conductance Matrices and Voltage Maps

Davide Pilati, Fabio Michieletti, Alessandro Cultrera, Carlo Ricciardi,*
and Gianluca Milano*

Self-organizing memristive nanowire (NW) networks are promising candidates for neuromorphic-type data processing in a physical reservoir computing framework because of their collective emergent behavior, which enables spatiotemporal signal processing. However, understanding emergent dynamics in multiterminal networks remains challenging. Here experimental spatiotemporal characterization of memristive NW networks dynamics in multiterminal configuration is reported, analyzing the activation and relaxation of network's global and local conductance, as well as the inherent spatial nonlinear transformation capabilities. Emergent effects are analyzed *i)* during activation, by investigating the spatiotemporal dynamics of the electric field distribution across the network through voltage mapping; *ii)* during relaxation, by monitoring the evolution of the conductance matrix of the multiterminal system. The multiterminal approach also allowed monitoring the spatial distribution of nonlinear activity, demonstrating the impact of different network areas on the system's information processing capabilities. Nonlinear transformation tasks are experimentally performed by driving the network into different conductive states, demonstrating the importance of selecting proper operating conditions for efficient information processing. This work allows a better understanding of the local nonlinear dynamics in NW networks and their impact on the information processing capabilities, providing new insights for a rational design of self-organizing neuromorphic systems.

1. Introduction

The field of neuromorphic engineering has attracted significant attention in recent years owing to its potential to revolutionize the design and development of electronic devices.[1–3] Thanks to their inherent capabilities of adapting to an external electrical stimulus, memristive systems, and devices have been adopted as artificial synapses for non-von Neumann computing architectures.[4–6] Besides conventional memristive architectures based on crossbar arrays,[7] self-organizing memristive networks of nanoscale elements have been shown to exhibit emergent behavior arising from the complex interaction among nanoelements.[8–10] This collective behavior has been demonstrated to emulate short-term/long-term synaptic plasticity effects, structural/wiring plasticity, memory engrams, and criticality.[11–15] The presence of neuromorphic features in these systems attracted great attention for the low-cost implementation of unconventional computing paradigms such as reservoir computing (RC).[9,12,16–25] The RC paradigm leverages the intrinsic spatiotemporal dynamics of a system (the reservoir) to map input to a feature space, outsourcing learning to a trainable readout layer. While the reservoir is conventionally modeled as a recurrent neural network, introducing a physical nonlinear, dynamic system as reservoir layer (from here the name Physical Reservoir Computing, or PRC) may open to hardware applications for a wide range

D. Pilati, F. Michieletti, C. Ricciardi
Department of Applied Science and Technology
Politecnico di Torino
Turin 10129, Italy
E-mail: carlo.ricciardi@polito.it

D. Pilati, G. Milano
Advanced Materials Metrology and Life Sciences Division
Istituto Nazionale di Ricerca Metrologica
Turin 10135, Italy
E-mail: g.milano@inrim.it

A. Cultrera
Quantum Metrology and Nanotechnologies
INRIM – Istituto Nazionale di Ricerca Metrologica
Turin 10135, Italy

ADVANCED
SCIENCE NEWS

www.advancedsciencenews.com

ADVANCED
ELECTRONIC
MATERIALS

www.advelectronicmat.de

of tasks.[26–28] In this context, the nonlinear dynamics of the physical system are exploited to extract spatiotemporal features of the input signal.[26,27]

However, the characterization and understanding of complex spatiotemporal emergent dynamics of these systems in multiterminal configuration still poses a challenge. Simulations have shown great PRC applicative potential, though using implementations that are difficult to obtain in experiments.[29] While in a simulation environment, it's easy to access an arbitrary number of signals from the reservoir to be used as reservoir outputs, experimentally assessing the internal state of the reservoir poses challenges. In this context, the number of reservoir signals that can be recorded is related to the number of terminals, i.e., to the hardware complexity.[30,31] Two terminal measurements have been used to characterize these systems in previous works,[8,13,32,33] as well as multiterminal measurement setups.[11,34] In the context of PRC implementations, different multiterminal setups and measurement strategies have been proposed for extracting information on the internal state of the physical network.[12,23,35] For example, Lissajous plots were exploited to investigate spatially distributed non-linear responses of self-organizing systems of Ag_2Se nanowires[35] and atomic switch networks.[36] However, conductance matrices and voltage maps were not investigated. In another work,[11] transresistance matrices of multiterminal devices have been acquired for mapping the spatial conductivity of NW networks. In this case, no information on the spatial distribution and evolution over time of voltage drop across the sample is provided.

In this work, we report on the spatiotemporal analysis of multiterminal memristive NW networks through the analysis of conductance matrices and voltage maps, allowing to monitor the emergent behavior of the system characterized by asynchronous activations and spatially distributed activity. The multiterminal characterizations provided information on the voltage spatial distribution while stimulating the network, allowing real-time monitoring of the emergent behavior, and reflecting the spatiotemporal evolution of the network functional connectivity upon electrical stimulation. While voltage maps allowed real-time monitoring during potentiation, conductance matrix analysis was exploited to analyze the network evolution during relaxation. We also reported a multiterminal nonlinear activity analysis, which showed how the choice of global conductive state impacts the information processing capabilities of the network.

2. Results and Discussion

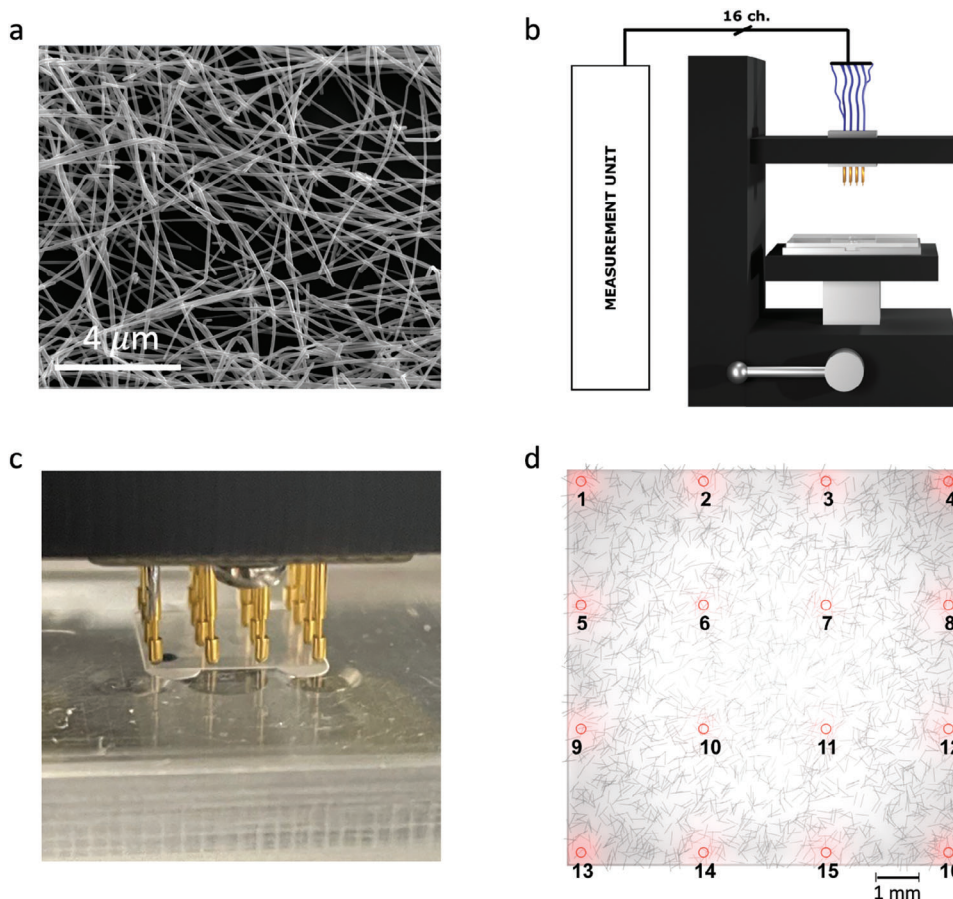### 2.1. Multiterminal Characterization of Memristive Nanowire Networks

Self-organizing NW networks were realized by drop-casting Ag NWs in solution on a quartz substrate (**Figure 1a**, Methods). The memristive switching mechanisms that regulate single-junction dynamics rely on the voltage-driven formation/rupture of Ag filaments penetrating the PVP insulating layer, which allows the junction resistance to adapt to external electrical stimuli, conferring inherent bio-synapse similarities in terms of electrical response.[14,5] The emergent behavior of these self-organized systems is exhibited through the collective operation

of memristive junctions and rewiring effects in single NWs,[37] conferring brain-like features to the network. In fact, when stimulated, the network shows some features typical of biological networks including homo and hetero-synaptic plasticity, structural plasticity, short- and long-term memory effects.[11,14] The electrical response results in being spatially distributed across the network, with different areas activating at different times.[8,10,15] Consequently, to characterize the spatiotemporal dynamics of these systems, a multiterminal approach is required.

The experiments described in this work were performed using a measurement board paired with a custom grid contact fixture (Figure 1b). The measurements were performed with an Arc Instruments ARC2 board,[38] which features fully parallel source measure unit (SMU) channels. For the experiments in this study, 16 of these channels were used. The selected channels were then connected to a custom grid setup which comprises a sample holder and a 4 × 4 grid of spring-loaded gold-plated contact pins (Figure 1c, details in Methods). Electrical contact was established by pushing the NW network sample against the gold pins, which allowed for direct electrical contact with the conductive Ag cores (Figure S1, Supporting Information).[32–34] The contact resistance in a similar setup has been studied in a previous work, and was determined to be negligible with respect to the network resistance in operating conditions (details in Methods).[39] The grid configuration of the contacts allows for monitoring the evolution of the system across the whole NW network area (Figure 1d). In all characterizations involving a single bias-ground configuration, electrode 1 (top left corner) was designated as the input, while electrode 16 (bottom right corner) was assigned as ground. This arrangement applies the voltage at two opposite corners, thereby distributing the electric field across the sample diagonal. Notably, this experimental setup allows real-time monitoring of voltage (or current) simultaneously in all electrodes, providing access to the spatiotemporal evolution of the network. Additionally, the measurement unit allows individual management of the electrical routing for each electrode, enabling independent biasing with a specific voltage, connection to ground, or designation as a floating electrode. With respect to state-of-the-art measurement setups,[11,24,19] where often waveform generation and voltage or current measurements are performed by two different units, this setup relies on parallel SMUs controlled by a single FPGA-based system, with no need of a switching matrix to change the electrode configuration. This enables rapid electrical measurement configuration switching, significantly minimizing the time required to perform such kind of measurements. Moreover, in neuromorphic networks, and particularly in NW networks, often the contacts are sputtered on the substrate to form contact pads.[23,24,19] The here-presented setup instead is capable of achieving electrical contact without the need of contact pads, enabling easier network characterization.[11]

2.2. Emergent Dynamics Through Conductance Matrices

The electrical connectivity of NWNs can be described through the conductance matrix of the multiterminal network, as previously investigated in ref. [40]. A conductance matrix is the result
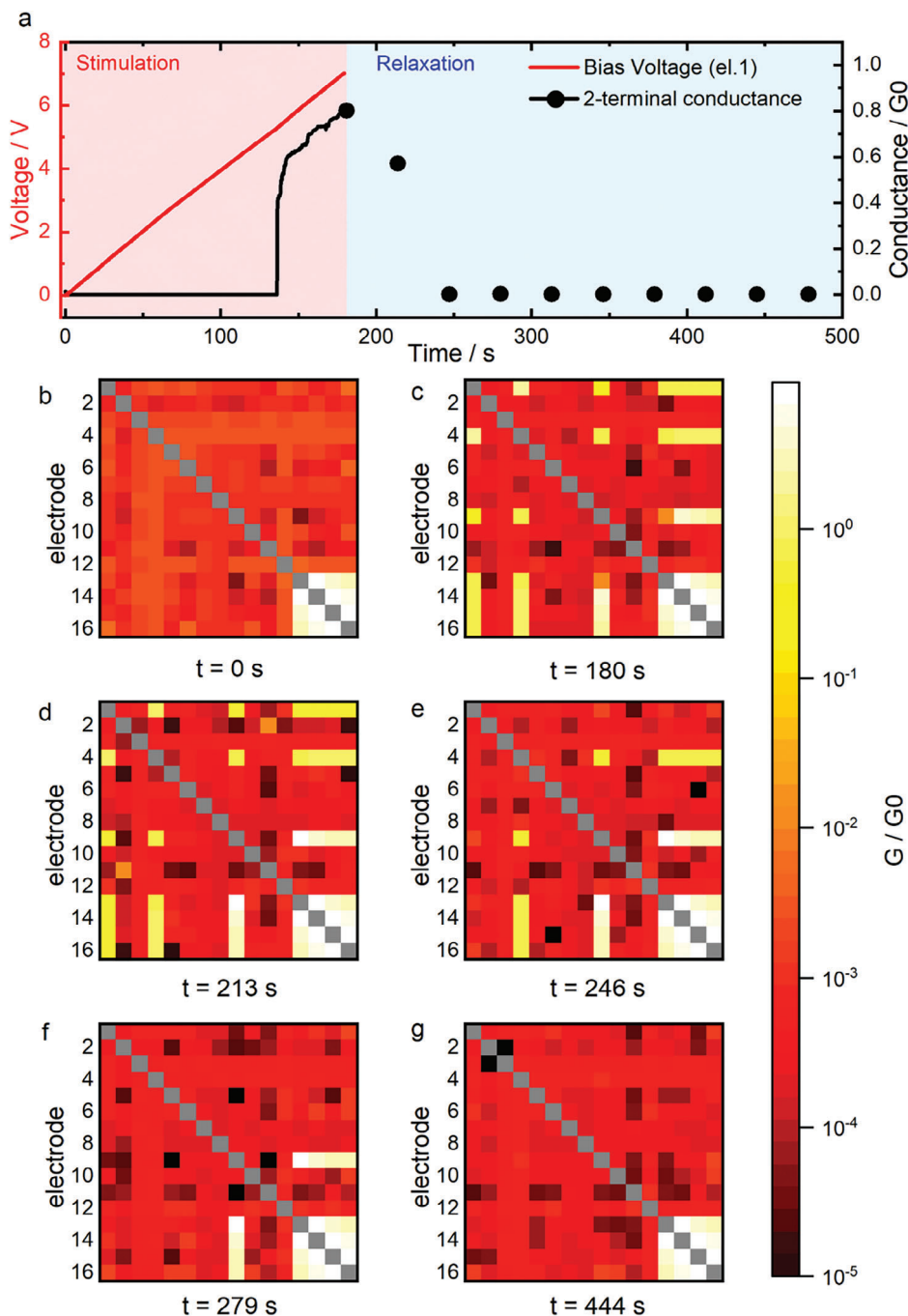
**ADVANCED
SCIENCE NEWS**

www.advancedsciencenews.com

**ADVANCED
ELECTRONIC
MATERIALS**
Open Access

www.advelectronicmat.de

Figure 1. Experimental Setup. a) SEM image of Ag NWN sample, scale bar is 4 µm. b) Measurement setup: sixteen channels from the Arc2 measurement board were connected to a 4 × 4 grid setup (16 pins). c) Spring-loaded pins in contact with the NWN sample. d) Pins position on NW network sample (sample size 1 × 1 cm²).

of a series of sequential two-terminal measurements, in which a reading voltage (100 mV) is imposed between the two electrodes and the resulting current is measured. Each element of the matrix corresponds to an electrode pair, and the value of each element is the effective network conductance seen by those two electrodes. The conductance matrix was used to determine the pristine state of the network (i.e., the conductive state before any electrical stimulus was applied), as well as for monitoring the potentiation and relaxation of the network under external stimulation (**Figure 2**). The network, which was initially found in the off state, was activated by applying a voltage stimulation ramp between selected electrodes placed across the diagonal (input voltage applied between electrodes 1 and 16, Figure 2a). From here on, we will refer to network turn-on (or network activation) as a significant increase in the global conductance (i.e., the effective conductance measured between a bias and a ground electrode positioned at opposite sample corners, i.e., respectively electrodes 1 and 16). After network activation, the voltage ramp was interrupted to monitor the spontaneous relaxation of the conductance state of the network both across the stimulated electrodes (Figure 2a) and in a multiterminal fashion by monitoring the evolution of the conductance matrix of the system (Figure 2b–g). It is worth noticing that, during the relaxation analysis, the reading voltage (100 mV) has been applied to the system just for the time needed to perform the conductance snapshots, avoiding any unnecessary stimulation. In the context of multiterminal analysis, the pristine-state conductance matrix depicted in Figure 2b reveals a conductive region distributed mainly across network areas probed by electrodes 13, 14, 15, and 16. This information is something unachievable with a standard two-terminal conductance measurement, such as the global conductance reported in Figure 2a, where only the conductance between the stimulated electrodes is available. The first conductance matrix measured after network stimulation (Figure 2c) shows the activation of electrodes 1, 4, and 9 as a consequence of network stimulation between electrodes 1 and 16. The potentiation measured by electrodes that have not been directly stimulated (e.g., electrodes 4 and 9) is a form of heterosynaptic plasticity.[14]

With regard to relaxation, the network takes ≈70 s to return to a turn-off state if considering the two-terminal conductance measurement across stimulated electrodes 1–16 (refer to Figure 2a). However, Figure 2e–g demonstrates that the network actually took significantly longer time (>260 s) to return to a state that resembles the pristine state (Figure 2g). This type of information is significant when implementing a series of experiments aimed

**ADVANCED
SCIENCE NEWS**

www.advancedsciencenews.com

**ADVANCED
ELECTRONIC
MATERIALS**
Open Access

www.advelectronicmat.de

Figure 2. Conductance matrix analysis. a) *I–V* ramp characterization showing potentiation and spontaneous relaxation over time. b) Pristine state conductance matrix. c) Conductance matrix after network potentiation. d-g) Conductance matrix analysis of the network relaxation over time.
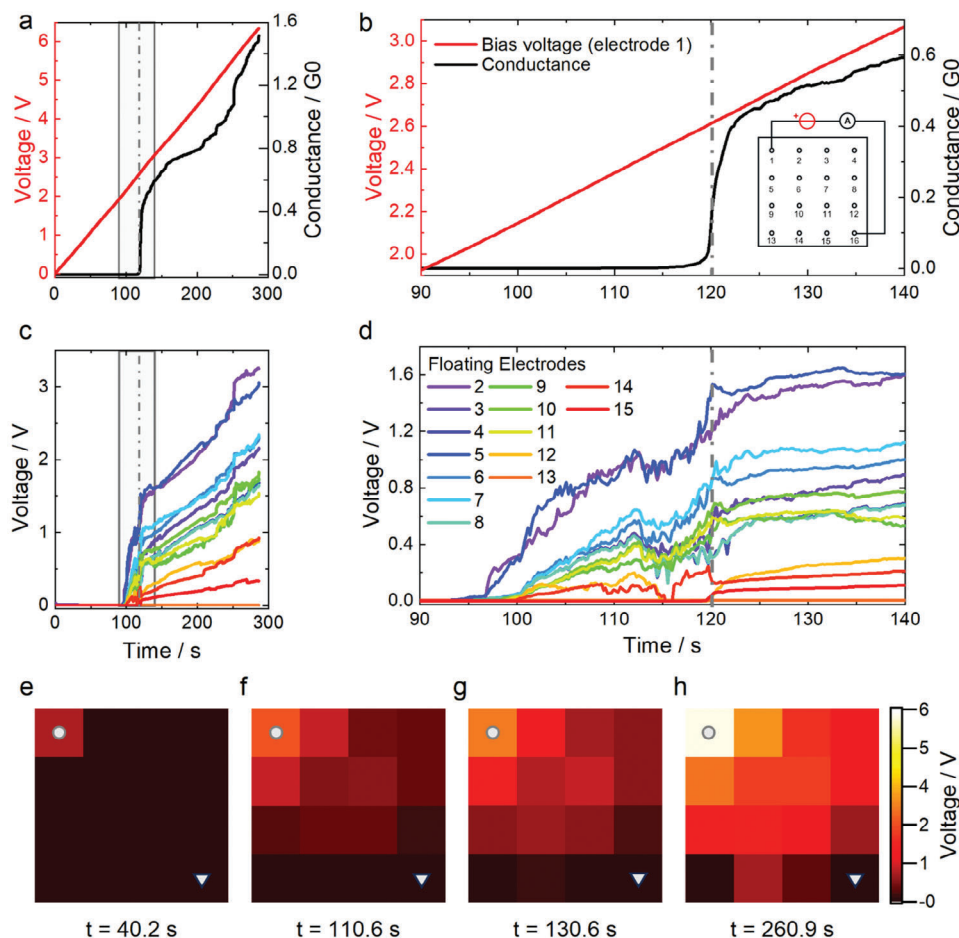
at operating in a multiterminal configuration, since results indicate that the relaxation of different network areas leads to differences in relaxation time of the effective conductance between different electrode pairs. Moreover, as demonstrated by the intermediate conductance matrices, internal rearrangements continue to occur until a conductance matrix similar to the pristine state is reached.

Although the conductance matrix provides information about the internal network connectivity, it cannot be used as a physi-

cal observable in a computing framework (e.g., RC), since this characterization technique does not allow synchronous measurements on all 16 electrodes.

2.3. Emergent Dynamics Through Voltage Maps

An alternative for investigating internal dynamics of the multiterminal network is represented by tracking the evolution of

**ADVANCED
SCIENCE NEWS**

www.advancedsciencenews.com

**ADVANCED
ELECTRONIC
MATERIALS**

www.advelectronicmat.de

Figure 3. Spatiotemporal analysis during I–V characterization. a) Input voltage and global conductance. b) Zoom of panel a around activation. c) Voltage evolution of floating electrodes. d) Zoom of panel c around activation. e—h) Spatial voltage distribution snapshots of the network during I–V characterization from e (t = 40.2 s) to h (t = 260.9 s). Bias electrodes in panels e–h are represented by a circle (source electrode) and a triangle (ground electrode).

voltage maps. These maps provide a visual representation of the spatial dynamics of the voltage distribution by presenting it as a heatmap, as shown in **Figure** 3e–h. In this case, the voltage (measured with respect to a ground electrode) is measured on all read electrodes that are kept floating, while the network is stimulated in two-terminal configuration between a source electrode and ground where also current is monitored (voltage and current sampling at 10 Hz). As reference, Figure 3a,b report the effective conductance measured between input and ground electrodes (normalized by the fundamental quantum of conductance G_0), when an external voltage is applied as stimulation in between electrode 1 and 16. While an activation is clearly revealed by a sudden jump in the global conductance between input and ground electrode occurring at $t = 120$ s, the two-terminal conductance does not provide information regarding the local voltage distribution, thus not helping in identifying localized effects. On the opposite, Figure 3c,d show that multielectrode voltage measurements allow real-time spatiotemporal dynamic analysis, differently from conductance matrices that are based on sequential measurements. It can be noticed that prior to activation, the effective conductance of the network between stimulated elec-

trodes exhibits intensified activity, as demonstrated by the spikes in the 90–120 s region (Figure 3d).[8,23] Such rapid fluctuations in the electrical activity are the typical fingerprint of metastable states related to the local dynamic reorganization of the network. Regarding localized dynamics, Figure 3d clearly shows the non-synchronous local activation of the different areas of the sample (represented by electrode pairs): while two electrodes (2 and 3) are activated around $t = 95$ s, other electrodes are organized in two groups that activate later (around $t = 100$ s and $t = 120$ s). Such experimental evidence about how information is spatiotemporally processed in a NWN would be unachievable with standard two-terminal sequential characterization set-ups.

The data provided by these measurements can be better visualized as time evolution of voltage maps, in which each square represents an electrode reflecting its spatial position on the sample. In the reported voltage maps (Figure 3e–h), although the effective conductance jump (network activation) between stimulated electrodes occurred at t = 120 s, electrodes 13, 14, and 15 remain electrically close to ground (electrode 16). This electrical configuration appears to be stable until t = 225 s, when the network begins to potentiate toward a higher conductive state, and

**ADVANCED
SCIENCE NEWS**

www.advancedsciencenews.com

**ADVANCED
ELECTRONIC
MATERIALS**

www.advelectronicmat.de

electrode 13 shows a voltage increase, suggesting activity in that area as a consequence of the formation of new conductive pathways or existing pathways adjustments in response to the input voltage increase. Given the voltage map reported in Figure 3h, we can observe that the voltage distribution across the sample area resembles a nearly homogeneous 2D material, but asynchronous jumps and fluctuations in local voltages are a direct consequence of emerging dynamics of the network. Thanks to these voltage maps, it is possible to analyze the behavior of the network during the activation phase since the measured activity is connected to the spatiotemporal dynamics of conductive paths formation (see voltage evolution from Figure 3e–h; Video S1, Supporting Information). Note that the movie format allows better visualization of the local activity of the network over time.

However, this approach comes with limitations. During active stimulation, this method allows a detailed study of conductive pathways formation, but during the relaxation phase the source voltage must be kept low (under 100 mV) to avoid stimulation. This results in a reduced applied voltage on the floating electrodes, with a consequent reduced signal-to-noise ratio that limits this characterization approach during the relaxation phase. While voltage maps enable to access the internal dynamics of the network during potentiation, the analysis of conductance matrix analysis remains a valid alternative to investigate conductance evolution during relaxation. These two characterization approaches can therefore be used in a complementary manner to investigate different aspects of the network electrical behavior: voltage maps provide a real-time snapshot that allows the investigation of local events such as spikes and asynchronous activations in terms of variations of voltage distributions, while conductance matrices allow the evaluation of electrode pair relations when sequential conductance matrices do not represent a limitation (i.e., during the slow spontaneous network relaxation). Moreover, while conductance matrices are purely used as a characterization tool, voltage maps can be also used to extract real-time voltage signals from different network areas for computing tasks such as nonlinear transformation (NLT) and, more in general, for physical reservoir computing applications.
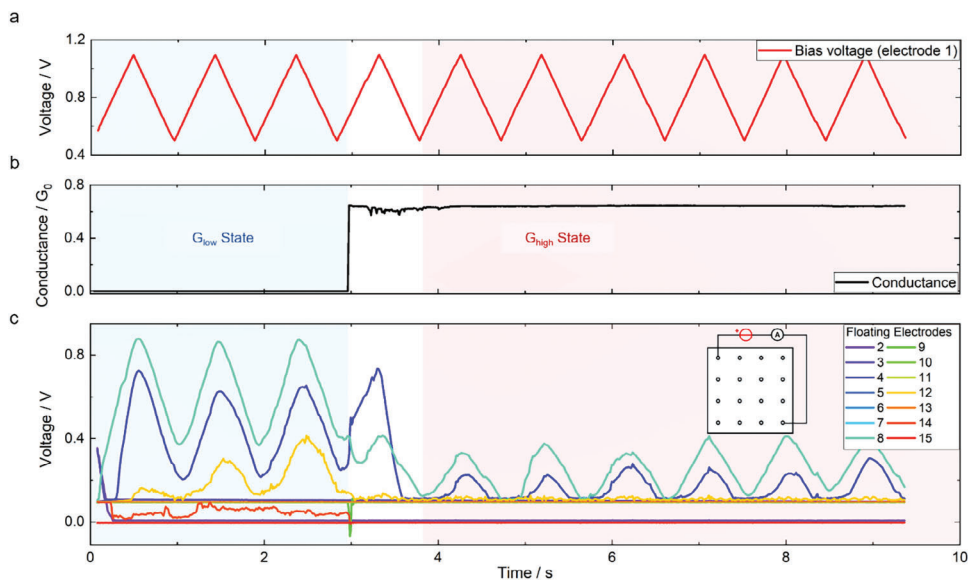
2.4. Nonlinear Response Analysis

In this section we report on local nonlinearity response of the network in different global conductance regimes, to study the influence of the system conductive state on its information processing capabilities. This has been done to demonstrate how emergent behavior can be exploited with the synchronous measurement methodology described previously in this work (volage maps) to perform reservoir computing, while simultaneously obtaining information about the system conductive state. However, it has to be clarified that the network has not been optimized for computing, since it is outside the scope of this work. For this purpose, the nonlinear transformation (NLT) task has been experimentally implemented, since it represents a common benchmark for analyzing the information processing capability of a physical network.[13,17,41,42] Here, the response of a nonlinear system is expected to be a periodic waveform in which the harmonic com-

ponents are changed with respect to the provided input (e.g., with a triangular wave fed as input, the network provides a sinusoidal wave as output). While it has been established that the dynamic condition of the system can influence NLT performance,[17] however, the ability to monitor the voltage evolution of all the electrodes simultaneously enables additional examination about the dynamic response variations. For this purpose, the voltage map (simultaneous sampling of the 16 electrode floating voltages) has been exploited as physical observable of the reservoir state for each timestep.

As illustrated in **Figure 4**, a triangular wave is fed to electrode 1 (Figure 4a), with electrode 16 at the other end of the diagonal set to ground. Conductance analysis was performed on these two electrodes (Figure 4b) to determine the global conductive state of the system, while the other 14 electrodes were set to floating state in order to read voltage (Figure 4c) and extract the output node signals (from the voltage readings only). The network showed activation between stimulated electrodes after 3 periods (Figure 4b), setting to a higher effective conductive state (0.6 G_0). For sake of clarity the low conductance region and the high conductance regions have been denominated respectively G_{low} state and G_{high} state. Following the network activation, the magnitude of the floating electrode voltages changes due to electrical reconfiguration of the network (Figure 4c). More interestingly, only few electrodes showed nonlinear response. Concerning nonlinear signals, Electrodes 4, 8, and 12 already provided a transformed output before the activation (G_{low} state), with their voltage evolutions resembling the shape of a sine wave. After a transition phase, in which the network turned on and adjusted itself to the new conductive state, the floating electrode outputs changed significantly. As shown in Figure 4c, around $t = 7$ s, the output waveform of electrode 8 exhibits a more pronounced triangular shape as the stimulation progresses, thereby worsening the inherent nonlinear transformation. On the other hand, remaining electrodes do not show resemblance to periodic waveforms, due to the inherent noisier characteristic of such low voltage signals (see Figure S2, Supporting Information for the zoomed graph).

Such a behavior is also supported by Lissajous patterns shown in **Figure 5**, where the electrode voltages are reported as a function of the input voltage for the G_{low} (Figure 5a) and for the G_{high} state (Figure 5b). Lissajous plots provide an immediate representation of the nonlinearity:[35,36] if an output signal is linearly dependent on a given input, the resulting plot will be a straight line, while a nonlinear dependence is represented by a circular shape. This analysis confirms that the electrodes showing a clear nonlinear response seem to be limited to electrode 4, 8, and 12. Furthermore it is possible to notice a worsening in the Lissajous patterns exhibited by electrodes 4, 8, and 12 as the system transitions from the G_{low} to the G_{high} state. This set of information is crucial for computing applications, since it demonstrates that the nonlinear contribution is not uniformly distributed across the sample area. The presented analysis not only shows that the nonlinear activity is confined to specific sample areas, but also highlights the significant influence that electrode selection can have on computational performance.

These observations were further corroborated by performing a series of non-linear transformation (NLT) tasks. From the triangular wave in input, the three targets for NLT performance

ADVANCED
SCIENCE NEWS

www.advancedsciencenews.com

ADVANCED
ELECTRONIC
MATERIALS

www.advelectronicmat.de

Figure 4. Nonlinear transformation analysis of a triangular wave. a) Input voltage as a triangular wave centered at 0.8 V with an amplitude of 0.6 V. b) Global conductance of the network evaluated between input electrode (1) and GND electrode (16). c) Voltage evolution of the floating electrodes. The transformation is modified upon global network activation.

assessment were a sinewave with the same period, a delayed triangular wave, and a square wave with the same period. In **Figure 6** we have reported a global overview of the NLT performances for all the aforementioned tasks. The predictions for the three tasks have been performed by means of linear regression, using the 14 signals from floating electrodes as reservoir output nodes (more details in Methods section). In Figure 6a–f both the targets (black lines) and the predicted waveforms (colored lines) are reported for the G_{low} (blue) and G_{high} (red) states. The accuracy for each task is shown in Figure 6g–i. From left to right, the tasks are reported in increasing difficulty order, and so the predictions get less and less accurate with respect to the targets. Interestingly, the network shows better performances before the activation (G_{low} state) for all the targets: sinewave (Figure 6a,d,g), phase shift (Figure 6b,e,h), and square wave task (Figure 6c,f,i).

To understand the impact of the nonlinear response of each electrode on computing performances, feature score maps were used (details in methods). Feature score represents a commonly employed method for feature selection in machine learning, utilized to individually evaluate features.[43] As can be observed from score maps for both G_{low} and G_{high} state reported in Figure 6j–o, not all electrodes impact the accuracy of the NLT task in the same way. Also, the impact of each electrode is different when considering different NLT tasks, suggesting that the local nonlinear response of the network could be optimized depending on the specific task. Furthermore, the impact of each electrode changes when the network is programmed in different networks states, further showing the importance of selecting proper operating conditions for efficient information processing.

3. Conclusion

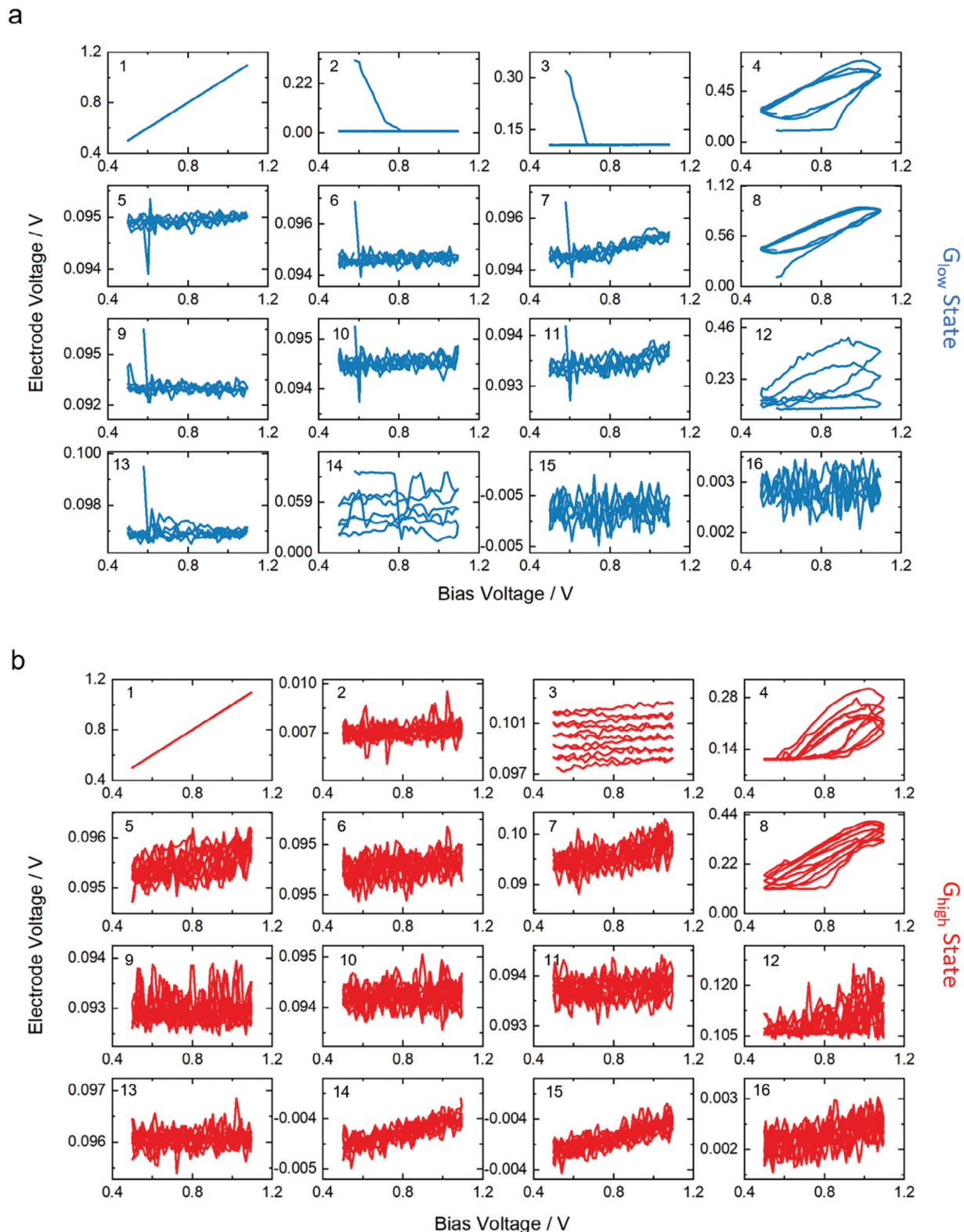We have demonstrated that multielectrode analysis of NWNs provides valuable information about the spatiotemporal evolution of emergent behavior, which is undetectable through traditional two-terminal measurements. This has been achieved by means of voltage maps, conductance matrices and multielectrode Lissajous nonlinear activity analysis. The results indicate that a two-terminal conductance analysis is only a manifestation of much more complex internal spatiotemporal dynamics that can be observed only with a multielectrode approach. Moreover, the results demonstrate that monitoring spatiotemporal voltage distribution can provide information on the formation and adaptation of conductive paths during the potentiation, revealing electrical activity that is not measurable with a conventional two-terminal setup. While conductance matrix analysis represents a valid solution for monitoring the relaxation over time, voltage maps acquired through synchronous measurements enable real-time monitoring of the potentiation phase. However, while we exploit reservoir computing as an example of how emergent behavior can be harnessed for computing, further work is required to optimize computing performances. Besides showing that different nonlinear responses can be observed in different network areas, results suggest that proper operation conditions are crucial for optimizing the computing performances of the system. More in general, these results shed new light on complex spatiotemporal dynamics arising from complexity in self-assembled nano systems, paving the way for more efficient implementations of physical reservoir computing.
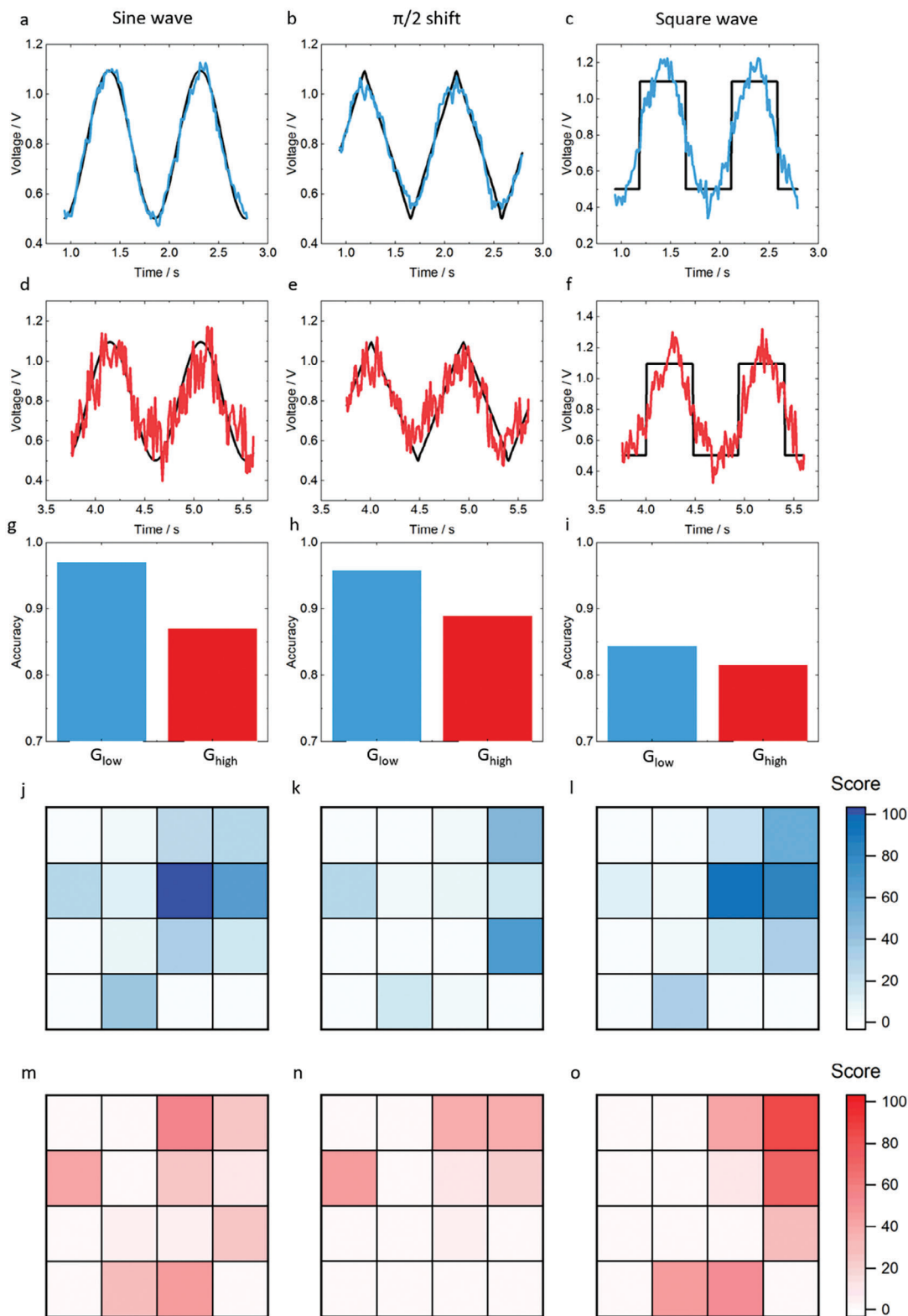
4. Experimental Section

NWN Fabrication: NWN were fabricated by drop-casting PVP-coated Ag nanowires (NW) in isopropyl alcohol (IPA) suspension (0.13%) on a quartz commercial substrate (1×1 cm^2).

The used nanowires were Sigma–Aldrich PVP-coated Ag NW, with length 20–50 µm and average diameter 115 nm ± 15 nm. The network density was controlled by diluting the NW suspension with additional IPA, starting from a product concentration of 0.5 wt.%. A 13.8 µL drop was

**ADVANCED
SCIENCE NEWS**

www.advancedsciencenews.com

**ADVANCED
ELECTRONIC
MATERIALS**
Open Access

www.advelectronicmat.de

Figure 5. Lissajous analysis of the nonlinear response of each electrode. a) Lissajous analysis before activation (G_{low} state). b) Lissajous analysis after activation (G_{high} state).

Figure 6. NLT performance overview. NLT tasks were performed by giving as input a triangular wave, while the targets were a same-period sinewave, a $\pi/2$ shifted triangular wave, and same-period square wave (first, second, and third column, respectively). a–f) Target (black lines) and prediction using G_{low} state and G_{high} state data (blue and red lines, respectively). g–i) Relative accuracies for the three targets, i.e., sinewave (g), shifted triangular wave (h), and square wave (i). j–o) Maps representing the feature score of each electrode for each task, for G_{low} (j–l) and G_{high} (m–o) state.

casted onto the substrate, and the IPA was removed by spontaneous evaporation. Fabrication parameters and respective densities were chosen following previous studies.[23,40]

Measurement Setup: The measurement setup was based on Arc Instruments ARC2 board.[38] ARC2 features 64 fully parallel SMU channels controlled by a FPGA. The instrument is controlled by a PC using custom-made Python scripts that exploit the exposed Rust libraries to control the board. The measurement board comes with a series of daughterboards that serve as interfaces for the SMU channels. The experiments conducted in this work have all been performed using 16 channels from the SMA 32 channel board. Custom SMA to DIN adapter cables have been made to bridge the measurement board with the 16 electrodes grid setup. The custom grid fixture has been realized on the base of previous experiences on electrical resistance tomography.[44] The fixture includes a insulating plastic sample holder and a movable contact array with 16 spring-mounted pins (Ingun GKS-080) disposed as a 4×4 grid. Pins' tips have a round profile with a radius of 400 μm. The movable contact array can be lowered to push the spring-loaded pins toward the NW and achieve direct, purely mechanical electrical contact between the pins and the Ag nanowire cores. Once the electrical contact is established, each individual channel can be independently connected to the voltage or current source, as well as left floating during the voltage reading. Moreover, each ARC2 channel can be connected to a hard ground, a soft ground, or the voltage source set to 0 V to be exploited as reference voltage.

Conductance Evaluation: The evaluation of the network's conductance was carried out as outlined in Equation (1), which is analogous to a two-terminal measurement between an input electrode and a ground electrode. This measurement was then normalized by the fundamental quantum of conductance, G_0, as per Equation (2). This is done for readability reasons, since the reported computing tasks are performed when the network is in a conductive state of the same order of magnitude as G_0.

$$G = \frac{I_{bias}}{V_{bias} - V_{GND}} \tag{1}$$

$$G_0 = \frac{2e^2}{h} = 7.748091729\ldots \times 10^{-5}\,\text{S} \tag{2}$$

In general, two terminal conductance measurements can be affected by contact resistance. The contact resistance between the spring-loaded pins and the nanowire network has been studied in a previous work,[39] finding a correlation between the contact resistances and the areal mass density (AMD). In particular, for AMD = 90 mg m^{-2}, the measured contact resistance was found to be less than 80 Ω. All the samples used in this work have higher AMD values, therefore resulting in a lower contact resistance with respect to the 90 mg m^{-2} samples. The operating conditions in this work are obtained for network resistances close to 10 kΩ, thus keeping the influence of the contact resistance lower than 1%.

Conductance Matrix Analysis: The conductance matrix was evaluated by computing the two-terminal conductance for each electrode pair. Being the measurement system globally controlled by the same FPGA, there is no need of external switching matrix or physical electrode reconfiguration to perform the measurement. The measurement is conducted at 40 Hz sampling rate, with each sample corresponding to a different electrode pair. The conductance for each electrode pair was determined following Equation (1), reading the current from the ground electrode with a bias voltage of 100 mV applied to the input electrode. The relaxation time of the NWNs under analysis has been demonstrated to be in the order of hundreds of seconds, therefore being able to perform an entire cycle of 112 measurements, each with a different electrode configuration, in just 3 s, allowing a significant analysis of the conductive state of the system.

Nonlinear Transformation (NLT) Tasks: The NLT tasks were performed starting from a triangular input signal centered on a bias voltage (0.8 V), with amplitude 0.3 V and frequency 1 ± 0.07 Hz, with measurement sampling frequency of ≈100 Hz. 14 output nodes were used by means of floating voltage measurements (16 total electrodes, including one source and one ground). The voltage readings from the output nodes were processed by a low-pass filtered designed in MATLAB with *designfilt* function (PB =

30 Hz, *SB* = 40 Hz, ripple = 1 dB, A_s = 12 dB). The filtered signals were used to train a linear regression model on three target signals: sinewave, phase-shifted triangular wave, and square wave. The accuracy for each target has been evaluated as 1-RNMSE, or Root Normalized Mean Square Error (Equation 3), as done by Fu et al. in a previous work.[17] Here, $T(t_n)$ represents the target value at time t_n, and $y(t_n)$ represents the reconstructed output, while N is the total number of samples.

$$RNMSE = \sqrt{\frac{\sum_{n=1}^{N}[T(t_n) - y(t_n)]^2}{\sum_{n=1}^{N}[T(t_n)]^2}} \tag{3}$$

The feature score of each electrode was evaluated through the MATLAB's built-in *fsrftest* function. This function assigns a score to each signal based on the F-test's p-value, following the equation below:

$$SCORE = -\log(\text{p-value}) \tag{4}$$

Supporting Information

Supporting Information is available from the Wiley Online Library or from the author.

Acknowledgements

Conflict of Interest

The authors declare no conflict of interest.

Data Availability Statement

The data that support the findings of this study are available from the corresponding author upon reasonable request.

Keywords

[1] D. V. Christensen, R. Dittmann, B. Linares-Barranco, A. Sebastian, M. Le Gallo, A. Redaelli, S. Slesazeck, T. Mikolajick, S. Spiga, S. Menzel, I. Valov, G. Milano, C. Ricciardi, S.-J. Liang, F. Miao, M. Lanza, T. J. Quill, S. T. Keene, A. Salleo, J. Grollier, D. Marković, A. Mizrahi, P. Yao, J. J. Yang, G. Indiveri, J. P. Strachan, S. Datta, E. Vianello, A. Valentian, J. Feldmann, et al., *Neuromorphic Comput. Eng.* **2022**, 2, 022501.

[2] A. Mehonic, A. J. Kenyon, *Nature* **2022**, *604*, 255.

[3] C. Kaspar, B. J. Ravoo, W. G. van der Wiel, S. V. Wegner, W. H. P. Pernice, *Nature* **2021**, *594*, 345.

[4] Z. Wang, H. Wu, G. W. Burr, C. S. Hwang, K. L. Wang, Q. Xia, J. J. Yang, *Nat. Rev. Mater.* **2020**, *5*, 173.

[5] S. H. Jo, T. Chang, I. Ebong, B. B. Bhadviya, P. Mazumder, W. Lu, *Nano Lett.* **2010**, *10*, 1297.

[6] Z. Wang, S. Joshi, S. E. Savel'ev, H. Jiang, R. Midya, P. Lin, M. Hu, N. Ge, J. P. Strachan, Z. Li, Q. Wu, M. Barnell, G.-L. Li, H. L. Xin, R. S. Williams, Q. Xia, J. J. Yang, *Nat. Mater.* **2016**, *16*, 101.

[7] Q. Xia, J. J. Yang, *Nat. Mater.* **2019**, *18*, 309.

[8] A. Diaz-Alvarez, R. Higuchi, P. Sanz-Leon, I. Marcus, Y. Shingaya, A. Z. Stieg, J. K. Gimzewski, Z. Kuncic, T. Nakayama, *Sci. Rep.* **2019**, *9*, 14920.

[9] A. Z. Stieg, A. V. Avizienis, H. O. Sillin, C. Martin-Olmos, M. Aono, J. K. Gimzewski, *Adv. Mater.* **2012**, *24*, 286.

[10] G. Milano, E. Miranda, C. Ricciardi, *Neural. Networks.* **2022**, *150*, 137.

[11] G. Milano, A. Cultrera, L. Boarino, L. Callegaro, C. Ricciardi, *Nat. Commun.* **2023**, *14*, 5723.

[12] A. Loeffler, A. Diaz-Alvarez, R. Zhu, N. Ganesh, J. M. Shine, T. Nakayama, Z. Kuncic, *Sci. Adv.* **2023**, *9*, 16.

[13] J. Hochstetter, R. Zhu, A. Loeffler, A. Diaz-Alvarez, T. Nakayama, Z. Kuncic, *Nat. Commun.* **2021**, *12*, 1.

[14] G. Milano, G. Pedretti, M. Fretto, L. Boarino, F. Benfenati, D. Ielmini, I. Valov, C. Ricciardi, *Adv. Intell. Sys.* **2020**, *2*, 2000096.

[15] A. Loeffler, R. Zhu, J. Hochstetter, A. Diaz-Alvarez, T. Nakayama, J. M. Shine, Z. Kuncic, *Neuromorphic Comput. Eng.* **2021**, *1*, 014003.

[16] R. K. Daniels, J. B. Mallinson, Z. E. Heywood, P. J. Bones, M. D. Arnold, S. A. Brown, *Neural. Networks.* **2022**, *154*, 122.

[17] K. Fu, R. Zhu, A. Loeffler, J. Hochstetter, A. Diaz-Alvarez, A. Stieg, J. Gimzewski, T. Nakayama, Z. Kuncic, *2020 International Joint Conference on Neural Networks (IJCNN)*, **2020**, 1-8.

[18] J. B. Mallinson, Z. E. Heywood, R. K. Daniels, M. D. Arnold, P. J. Bones, S. A. Brown, *Nanoscale* **2023**, *15*, 9663.

[19] J. B. Mallinson, J. K. Steel, Z. E. Heywood, S. J. Studholme, P. J. Bones, S. A. Brown, *Adv. Mater.* **2024**, *36*, 2402319.

[20] H. O. Sillin, R. Aguilera, H. H. Shieh, A. V. Avizienis, M. Aono, A. Z. Stieg, J. K. Gimzewski, *Nanotechnology* **2013**, *24*, 384004.

[21] H. Tanaka, S. Azhari, Y. Usami, D. Banerjee, T. Kotooka, O. Srikimkaew, T. T. Dang, S. Murazoe, R. Oyabu, K. Kimizuka, M. Hakoshima, *Neuromorphic Comput. Eng.* **2022**, *2*, 022002.

[22] T. T. Dang, O. Srikimkaew, D. Banerjee, S. Azhari, Y. Usami, H. Tanaka, *Appl. Phys. Lett.* **2024**, *124*, 91903.

[23] G. Milano, G. Pedretti, K. Montano, S. Ricci, S. Hashemkhani, L. Boarino, D. Ielmini, C. Ricciardi, *Nat. Mater.* **2021**, *21*, 195.

[24] R. Zhu, S. Lilak, A. Loeffler, J. Lizier, A. Stieg, J. Gimzewski, Z. Kuncic, *Nat. Commun.* **2023**, *14*, 6697.

[25] G. Milano, K. Montano, C. Ricciardi, *J Phys D Appl Phys* **2023**, *56*, 084005.

[26] K. Nakajima, *Jpn. J. Appl. Phys.* **2020**, *59*, 060501.

[27] G. Tanaka, T. Yamane, J. B. Héroux, R. Nakane, N. Kanazawa, S. Takeda, H. Numata, D. Nakano, A. Hirose, *Neural. Networks.* **2019**, *115*, 100.

[28] X. Liang, J. Tang, Y. Zhong, B. Gao, H. Qian, H. Wu, *Nat. Electron.* **2024**, *7*, 193.

[29] J. Love, R. Msiska, J. Mulkers, G. Bourianoff, J. Leliaert, K. Everschor-Sitte, *Phys. Rev. Appl.* **2023**, *10*, 044057.

[30] Z. Kuncic, O. Kavehei, R. Zhu, A. Loeffler, K. Fu, J. Hochstetter, M. Li, J. M. Shine, A. Diaz-Alvarez, A. Stieg, J. Gimzewski, T. Nakayama, *2020 IEEE International Symposium on Circuits and Systems (ISCAS)*, **2020**, 1-5.

[31] Z. Kuncic, T. Nakayama, *Adv Phys X* **2021**, *6*, 1894234.

[32] H. G. Manning, F. Niosi, C. G. da Rocha, A. T. Bellew, C. O'Callaghan, S. Biswas, P. F. Flowers, B. J. Wiley, J. D. Holmes, M. S. Ferreira, J. J. Boland, *Nat. Commun.* **2018**, *9*, 3219.

[33] Q. Li, A. Diaz-Alvarez, R. Iguchi, J. Hochstetter, A. Loeffler, R. Zhu, Y. Shingaya, Z. Kuncic, K. Uchida, T. Nakayama, *Adv. Funct. Mater.* **2020**, *30*, 2003679.

[34] A. Diaz-Alvarez, R. Higuchi, Q. Li, Y. Shingaya, T. Nakayama, *AIP Adv.* **2020**, *10*, 025134.

[35] T. Kotooka, Y. Tanaka, H. Tamukoh, Y. Usami, H. Tanaka, *Appl. Phys. Express* **2023**, *16*, 014002.

[36] K. S. Scharnhorst, J. P. Carbajal, R. C. Aguilera, E. J. Sandouk, M. Aono, A. Z. Stieg, J. K. Gimzewski, *Jpn. J. Appl. Phys.* **2018**, *57*, 03ED02.

[37] G. Milano, F. Raffone, K. Bejtka, I. De Carlo, M. Fretto, F. C. Pirri, G. Cicero, C. Ricciardi, I. Valov, *Nanoscale Horiz.* **2024**, *9*, 416.

[38] P. Foster, J. Huang, A. Serb, S. Stathopoulos, C. Papavassiliou, T. Prodromakis, *Sci. Rep.* **2022**, *12*, 13912.

[39] G. Milano, A. Cultrera, K. Bejtka, N. De Leo, L. Callegaro, C. Ricciardi, L. Boarino, *ACS Appl. Nano Mater.* **2020**, *3*, 11987.

[40] G. Milano, G. Pedretti, M. Fretto, L. Boarino, F. Benfenati, D. Ielmini, I. Valov, C. Ricciardi, *Adv. Intell. Sys.* **2020**, *2*, 2000096.

[41] E. C. Demis, R. Aguilera, K. Scharnhorst, M. Aono, A. Z. Stieg, J. K. Gimzewski, *Jpn. J. Appl. Phys.* **2016**, *55*, 1102B2.

[42] M. Takayanagi, D. Nishioka, T. Tsuchiya, M. Imura, Y. Koide, T. Higuchi, K. Terabe, *Mater. Today. Adv.* **2023**, *18*, 100393.

[43] N. Omer Fadl Elssied, O. Ibrahim, A. H. Osman, *Res. J. Appl. Sci., Eng. Technol.* **2014**, *7*, 625.

[44] A. Cultrera, D. Serazio, A. Zurutuza, A. Centeno, O. Txoperena, D. Etayo, A. Cordon, A. Redo-Sanchez, I. Arnedo, M. Ortolano, L. Callegaro, *Sci. Rep.* **2019**, *9*, 10655.